Mechanics of Metal-Nanocomposites at Multiple Length Scales: Case of Al-BNNT

N. M. Anoop Krishnan[1] and Debraj Ghosh[2]

Abstract: Metal-nanocomposites are drawing attention of the composites community due to improvements in stiffness, strength, crack-bridging ability, and resistance to creep and fracture. The analysis of nanocomposites involves studies at multiple length scales due to the small length of the reinforcement. This paper conducts a detailed study on the mechanical behavior of a metal nanocomposite (Al-BNNT)—made of an aluminum (Al) matrix reinforced with boron nitride nanotubes (BNNTs)—under compressive and shear loadings. First a representative volume element (RVE) is modeled and analyzed using molecular dynamics (MD) simulation. Then the elastic properties are derived for a specially orthotropic lamina using a hierarchical multiscale scheme in conjunction. This result is further extended to derive elastic and shear moduli of bulk nanocomposites with aligned and randomly oriented reinforcement. The result shows excellent agreement with previous experimental observations. The bounds of elastic moduli using Voigt and Reuss formulations diverge with an increase in volume fraction of reinforcement—unlike typical composites, in which these two bounds first diverge and then eventually converge. This anomaly is attributed to the weakness of nanotubes in the radial direction. However, most elastic properties are found to be improved by the reinforcement, especially by double-walled nanotubes. Depending on the type of loading, nanocomposite exhibits failure at the matrix, interface, or nanotubes. This reveals the importance of considering all three loading cases when modeling a nanocomposite. **DOI: 10.1061/(ASCE)NM.2153-5477.0000129.**

Author keywords: Metal nanocomposites; Elastic modulus; Nanotube reinforcement; Mixture rule.

Introduction

Because of their exceptional strength and unique mechanical properties, nanotubes are considered as prospective reinforcements to design lighter, stronger, and stiffer composites that exhibit pronounced resistance to temperature variations, fracture (Zhan et al. 2003; Gojny et al. 2004), and creep (Ajayan et al. 2006; Yang et al. 2007) In the regime of traditional (macro) composites, continuous fibers are favored over discontinuous fibers as reinforcement in critical applications due to better stiffness and strength. On the other hand, discontinuous fibers impart a nearly isotropic behavior and higher workability. Stiffness, strength, and workability can be achieved together in nanocomposites (Pogrebnjak and Beresnev 2012; Ivashchenko et al. 2014) due to the superior properties and smaller size of nanotubes. Primarily there are three matrix materials in nanocomposites: polymer, ceramic, and metal. Polymer-nanocomposites have been under active development for the last few years, including successful commercial applications (Coleman et al. 2006), due to the relative ease of manufacturing and pronounced improvement in bulk properties such as stiffness. Similarly, ceramic-nanocomposites also have been used in various practical applications such as biomedical engineering and wear-resistant materials (Porwal et al. 2013) due to improved fracture toughness and the nanotubes' crack-bridging ability. Recent developments in manufacturing technology have led to a surge of interest in developing metal-nanocomposites (Bakshi et al. 2010; Camargo et al. 2009; He et al. 2009; George et al. 2005; Pogrebnjak et al. 2014), with the primary goal of improving strength and stiffness. Moreover, reinforcing metal with nanotubes can improve the resistance to creep (Han et al. 2012), thermal elongation (Camargo et al. 2009), and fracture (Kim et al. 2007). Although a number of experimental studies have reported on metal-nanocomposites, there are very few reported analytical and computational studies. This paper conducts a detailed study of the mechanics of metal-nanocomposite in a multiscale framework ranging from atomistic simulation to continuum mechanics. The intention is to highlight the primary differences between the mechanics of traditional composite and nanocomposite.

Aluminum, due to its light weight, has emerged as a popular choice for the matrix (Silvestre 2013). Both carbon and boron nitride nanotubes (CNTs and BNNTs, respectively) have been used as the reinforcement. Whereas CNTs have a tendency to agglomerate and form bundles in a composite (Herasati and Zhang 2014), BNNTs give a relatively straight shape due to their partial ionic character and preferential B–N–B–N stacking (Yamaguchi et al. 2013). Therefore special techniques for obtaining a homogeneous distribution of CNTs in the composites—such as nanoscale dispersion (Noguchi et al. 2004), in situ chemical vapor decomposition (He et al. 2007, 2009), and mechanical alloying (Esawi and Morsi 2007)—are not required for BNNT reinforcement. Boron nitride nanotubes are chemically and thermally more stable than CNTs (Moon and Hwang 2004; Sekkal et al. 1998), and therefore can be used at elevated temperatures without damaging the structure of the reinforcement and the composite. Therefore stable nanocomposites with relatively uniform dispersion of reinforcement can be achieved using BNNTs as reinforcements.

There are only a few experimental studies on metal composites reinforced with BNNT. Yamaguchi et al. (2012) synthesized and

[1]Graduate Student, Dept. of Civil Engineering, Indian Institute of Science, Bangalore, Karnataka 560012, India (corresponding author). ORCID: https://orcid.org/0000-0003-1500-4947. E-mail: anoopnm@civil.iisc.ernet.in

[2]Associate Professor, Dept. of Civil Engineering, Indian Institute of Science, Bangalore, Karnataka 560012, India. E-mail: dghosh@civil.iisc.ernet.in

Note. This manuscript was submitted on October 30, 2015; approved on March 14, 2017; published online on September 22, 2017. Discussion period open until February 22, 2018; separate discussions must be submitted for individual papers. This paper is part of the ***Journal of Nanomechanics and Micromechanics***,

analyzed the structural and mechanical properties of an aluminum matrix reinforced with BNNTs. They revealed that the Al-BNNT nanohybrid can withstand approximately nine times greater stresses than can pure Al. This observation promised a new direction in the research of metal-nanotube nanocomposites. They later extended their study to fabricate lightweight aluminum ribbons reinforced with multiwalled (MW) BNNTs and found that at room temperature the ultimate tensile strength of Al ribbons with BNNTs was twice that of a pristine Al ribbon. Lahiri et al. (2012) studied the feasibility of using BNNT as a reinforcement instead of CNT for the aluminum matrix and the role of the reaction products formed at the interface in ensuring a strong bonding. In a follow-up work, Lahiri et al. (2013) further fabricated the BNNT-Al nanocomposite by plasma sintering. They studied mechanical properties, the microstructure, and the deformation behavior of the nanocomposite for different concentrations of BNNTs. They observed an almost 50% improvement in the compressive strength, and high deformability without a failure of the matrix. The BNNTs were observed to survive high temperature and pressure conditions during the sintering process, and large deformation during cold rolling.

The length scale of the building block in nanocomposite demands the use of computational methods such as first-principle calculation and molecular dynamics (MD) simulation. Results from these calculations then need to be scaled to the continuum range to find bulk properties. First-principle calculations such as density functional theory (DFT) and ab initio MD involve electronic structure calculations. Thus they are computationally expensive, even for a small number of atoms. Therefore the use of ab initio methods is limited to calibrating the interatomic potential and characterizing the interface. Song and Zha (2010) investigated the mechanical behavior of Ni-coated single-walled (SW) CNTs embedded in an aluminum matrix using MD simulations. They also investigated the effect of Ni-coating on the interfacial bonding and load transfer in a nanocomposite. Silvestre et al. (2014) studied the compressive behavior of CNT-reinforced aluminum composites using MD simulations and revealed that although the CNTs make the composite stronger, they buckle even in the embedded matrix under compressive loading. Kim et al. (2011) proposed a multiscale method to analyze the mechanical behavior of aluminum based metal-matrix nanocomposites. Bernhardt (2014) studied the wetting of BNNT by aluminum using DFT simulations and determined that strong binding can be obtained between aluminum and BNNT, suggesting the potential of BNNT-Al nanocomposite.

Based on the literature review, two areas are identified that require attention: (1) determining the differences between nanocomposite reinforcement and traditional fiber-reinforced composites, and accordingly extending the theory of composite materials to include nanocomposites; and (2) studying the interfacial strength of Al-BNNT and failure mechanisms occurring in nanocomposites.

This paper addresses these two issues in a multiscale framework coupling quantum, molecular, and continuum scales. Multiscale methods can be classified as hierarchical or information passing or as concurrent (Fish 2009). In a hierarchical multiscale method, the information at a finer length scale is used to generate the model at a coarser length scale (Liu et al. 2006). The information passing generally is carried out through a homogenization scheme. In contrast, in a concurrent multiscale method, the simulations at different length scales are performed simultaneously. Miller and Tadmor (2009) compared fourteen multiscale method. The current paper uses a hierarchical multiscale scheme with a systematic information passing from quantum to molecular to continuum scales to analyze BNNT-reinforced Al nanocomposite. Accordingly, mechanical properties of a representative volume element (RVE) are studied using MD simulation. Matrix–nanotube interface properties are characterized using first-principle calculations. Bulk properties of the nanocomposite such as constitutive relations then are derived from these results using continuum mechanics. One key finding of this work is that the radial weakness of the reinforcements—due to the hollow tubular structure—leads to a significant departure from the underlying mechanics of traditional nanocomposites. This departure manifests in the elastic properties and failure strength. Estimates from Voigt and Reuss mixture rules are found to diverge as the volume fraction of the reinforcement increases. The number of walls and direction of loading in BNNTs also are found to play an important role in the failure mechanism of nanocomposite.

This paper first explains the molecular simulation and density functional theory used to model the nanocomposite, followed by the theoretical framework used to analyze the nanocomposite. Results obtained from MD simulations and related discussions are presented next. Finally, concluding remarks of the present work and its practical relevance are mentioned in the last section.

MD Simulation

The nanocomposite was modeled using a RVE approach. The reinforcements were considered to be aligned in one direction. Hence, two of the three orthogonal directions (Directions 1 and 2 in Fig. 1) in the RVE were equivalent. This means that the application of a stress in one or two directions, independently, should yield the same overall response. The RVE, when extended periodically in two directions, yielded a nanocomposite lamina. With randomly oriented nanotubes as reinforcements, a nanocomposite with nearly isotropic behavior can be obtained.

Simulation Details and Stress Calculation

The RVEs for pure aluminum and the nanocomposite were modeled separately using *LAMMPS* (Plimpton 1995) and *VMD* (Humphrey et al. 1996). The simulation box had the dimensions $40.5[100] \times 40.5[010] \times 81[001]\text{Å}^3$ with a periodic boundary condition enforced in all three directions. The aluminum crystal was modeled as an FCC lattice with the lattice parameter 4.05 Å. The reinforcements used were (10,10) BNNT for SWBNNT and (7,7)@(10,10) for double-walled (DW) BNNT. The reinforcement weight percentage corresponded to 7.59 and 10.92% in the case of SWBNNT and DWBNNT, respectively. Similarly, the percentage volume of the reinforcement was 7.11%. Note that the volume percentage of both SWBNNTs and DWBNNTs was the same because the hollow volume is included in the reinforcement volume.

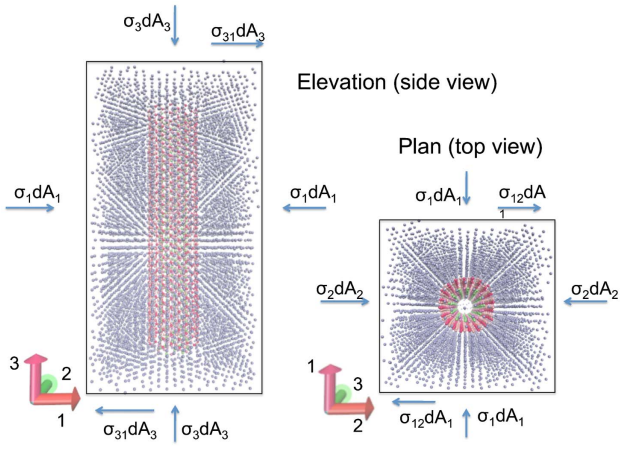

Fig. 1. RVE with a DWBNNT as reinforcement

Varying percentage and embedded length of reinforcement could have a significant effect on the stress transfer and overall properties of the nanocomposite. This paper limited the length and volume percentage to 7.11% in order to identify the effect of the number of walls of the reinforcement in the nanocomposite and the corresponding failure mechanisms in each case.

Once the initial coordinates were given as the input, the system was allowed to equilibrate by running the simulation for 10 ps. The time-step used for integrating the equation of motion was 1 fs. The time integration was performed on an isothermal-isobaric (NPT) ensemble, at 300 K and 0 Pa, using a Nosé–Hoover thermostat. After equilibration, the new box dimension was saved. The new box dimensions were very close to those of the initial structure. For improved accuracy, the new dimensions were used to obtain the Poisson's ratio. A constant strain then was applied by deforming the simulation box in the desired direction. Fig. 1 shows the RVE of the aluminum matrix with a DWBNNT reinforcement. In the case of uniaxial compression, the strain was applied by moving the opposite walls of the simulation box toward each other. This simulation was carried out in the x and z directions separately. For shear strain, the opposite walls in the same plane were moved parallel to each other. It was ensured that the walls moved in opposite directions in order to avoid rigid-body motion. This shear strain was applied in the x-z and x-y directions separately. The directions corresponding to each strain can be inferred from Fig. 1. A displacement rate of 0.1 Å/ps was used in all cases. The stresses corresponding to each direction are marked clearly in this figure. Note that the stresses represented in this figure show all possible stresses and not those corresponding to any particular simulation. Poisson's ratio can be calculated using the applied strain and relative change in the size of the simulation box. The stress in the desired direction at each step was evaluated using the virial definition (Subramaniyan and Sun 2008) of stress. The virial stress, when averaged over space and time, converges to the Cauchy stress tensor. The virial stress is of the form

$$\sigma_{ij} = \frac{1}{V}\left[\sum_{A=1}^{N} -m_A v_{A,i} v_{A,j} + \frac{1}{2}\sum_{A=1}^{N}\sum_{B=1,B\neq A}^{N} \frac{\partial\phi(r)}{\partial r}\frac{r_i r_j}{r}\bigg|_{r=r_{AB}}\right] \quad (1)$$

where V = total volume; m_A and v_A = mass and velocity, respectively, of atom A; N = number of atoms in volume V; ϕ = interatomic potential; r_i and r_j = position vectors; and r_{AB} = relative position of atom B with respect to atom A.

Modeling RVE

To model the RVE, a cylindrical void was created in the simulation box with the centers of the void and the simulation box coinciding. The radius of this void was chosen to be 3.4 Å more than the radius of the BNNT to be inserted. This choice ensured that a distance of 3.4 Å was maintained between the nanotube wall and the matrix to prohibit any premature breaking of the reinforcement. The BNNT was inserted in the void enclosed by the aluminum matrix on all sides. An equilibrium distance of 3.4 Å was used as the spacing between the BNNT and the aluminum. The case of a SWBNNT used a (10,10) armchair BNNT, whereas the case of a DWBNNT used a {(7,7)@(10,10)} BNNT. The embedded-atom method (EAM) potential with the parameters proposed by Winey et al. (2009) was used to model the interactions among the aluminum atoms. According to the EAM potential, the potential energy E_i of an atom i is of the form

$$E_i = \sum_{j=1}^{N} \phi(r_{ij}) + f(\rho_i) \quad (2)$$

where ρ_i = local electron density; and f = embedding function. The embedding function describes the dependence of the energy of an atom on the local electron density. Thus the embedding function is a multibody term which incorporates the effect of the local environment on the energy of the atom. This potential was shown to be effective in modeling metallic aluminum under different temperature conditions. The interactions for a BNNT were described using the three-body Tersoff potential with the interaction parameters proposed by Sevik et al. (2011).

However, there were no potentials available to model the interactions between the aluminum matrix and BNNTs. A common choice would be Lennard-Jones (LJ) 12-6 potential (Silvestre et al. 2014). However, the interaction parameters such as the equilibrium distance and energy need to be estimated to model this potential. Quantum mechanical simulations, otherwise known as the first-principle simulations, were used to this extent.

Mechanics and Modeling of Interface

To characterize the interface between BNNT and aluminum, first-principles density functional theory with dispersion-corrected (DFT-D) calculations were conducted using DMol3 in *Materials Studio* (Delley 1990, 2000). The binding energy of aluminum and BNNT cluster was estimated by geometry optimization. The number of aluminum atoms was restricted to one to reduce the computational cost. Gradient corrected functional form with Perdew–Burke–Ernzerhof (Perdew et al. 1996) (PBE) exchange-correlation functional were used. Long-range dispersion correction was carried out via Grimme's scheme. Spin-unrestricted DFT with formal spin as an initial condition was used because the spin could play an important role in the case of isolated atoms and small clusters. All electron core treatment was provided. Double numerical atomic orbital augmented by d-polarization functions (DNP) basis sets were used for solving self-consistent field (SCF) equations to provide better accuracy. Convergence thresholds for the optimization were fixed as 10^{-5} Ha for energy, 0.002 Ha/Å for force, and 0.005 Å for displacement. The binding energy of BNNT-Al cluster was found to be 0.909 eV. This binding energy is very low compared with cases of ionic or covalent bonds, for instance. Therefore the weak interaction at the interface can be attributed to the van der Waals forces, and can be modeled using a 12-6 LJ potential. It should be noted that the binding energy obtained from a BNNT-Al cluster with a single Al atom might not correspond to the exact interfacial energy, because the Al atom behaves differently in bulk and in isolation. However, the low values of binding energy obtained from the study are representative of the weak interaction between the Al atoms and the BNNT. As such, the DFT simulations justified the use of an LJ-potential to model the interface.

Furthermore, defects such as Stone–Wales (Li et al. 2008) and vacancy (Zobelli et al. 2007) were found to affect the strength and stiffness of the nanotubes (Krishnan and Ghosh 2014). This could in turn affect the properties of the nanocomposite. A detailed study of the effect of vacancy defects on the interfacial strength is proposed as a future work. The binding energies of clusters of B-vacancy, N-vacancy, and pristine BNNTs with an aluminum atom were obtained by simulation. The binding energy, BE, is determined as

$$\mathrm{BE} = \mathrm{EE}_{\mathrm{Al-BNNT}} - (\mathrm{EE}_{\mathrm{BNNT}} + \mathrm{EE}_{\mathrm{Al}}) \quad (3)$$

where EE = equilibrium energy. Furthermore, the equilibrium distances from the Al atom to all the atoms in the BNNT was calculated. A cutoff of 8 Å was used while calculating the distances. Assuming an LJ-type form, the weighted average of the potential energy with the distance was equated to the total binding energy.

Table 1. Values of β and α according to the LB Mixing Rule

Element 1	Element 2	α (eV)	β (Å)
Al	N	0.0511	2.993
Al	B	0.0414	3.036
B	B	0.0041	3.453
N	N	0.0063	3.365
B	N	0.0051	3.409

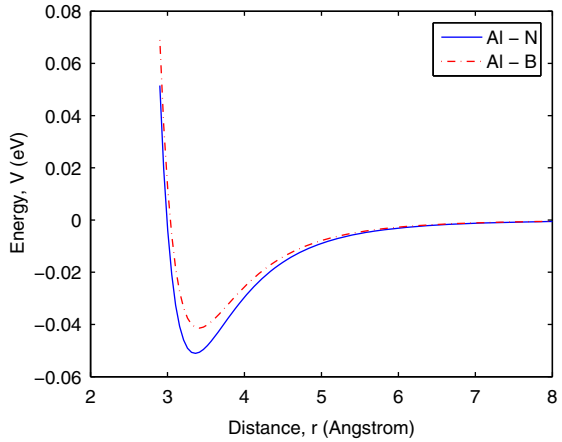

Fig. 2. LJ potential of Al-B and Al-N interaction obtained using the mixture rules; the binding energy obtained from DFT calculation is −0.045 eV

Thus the binding energy corresponding to the equilibrium distance was obtained as −0.045 eV.

The LJ potential used to model the interface between the aluminum and the BNNT is given by

$$V = 4\alpha\left[\left(\frac{\beta}{r}\right)^{12} - \left(\frac{\beta}{r}\right)^{6}\right] \tag{4}$$

where V = potential energy of two interacting particles; α = well depth of the potential; β = nontrivial distance at which the interparticle potential is zero; and r = distance between the interacting particles. For heterogeneous mixtures, the appropriate values of the parameters β and α can be obtained using various mixing rules such as the Lorentz–Berthelot (LB), Halgren HHG, and Waldman–Hagler rules. This paper used the LB mixing rules, which are widely used (Allen et al. 1987; Silvestre et al. 2014) to model the van der Waals interaction for heterogeneous materials. According to the LB mixing rule

$$\beta_{ij} = \frac{1}{2}(\beta_{ii} + \beta_{jj}), \qquad \alpha_{ij} = \sqrt{\alpha_{ii}\alpha_{jj}} \tag{5}$$

where i and j refer to different elements.

Table 1 gives the values of β and α obtained using the LB mixing rule. Fig. 2 plots the LJ potential thus obtained. The binding energy for a pair of atoms obtained from DFT calculation of a BNNT-Al cluster was −0.045 eV. Thus the mixing rule is in good agreement with the DFT calculation. Note that the LJ parameter for CNT-Al nanocomposite was reported as −0.035 eV (Silvestre et al. 2014). Thus the interfacial strength for BNNT-Al nanocomposite was higher than that of corresponding CNT-Al nanocomposite. The interaction between the concentric BNNTs in a DWBNNT was modeled using LJ potential as well, although with different interaction parameters, as shown in Table 1.

Mechanics of Nanocomposite Lamina

Using the theory of composite materials, this section describes the constitutive relation of aligned and randomly oriented fiber composites. Molecular dynamics simulation results serve as the basis for extending these relations to the nanocomposite.

Fig. 3 shows the nanocomposite lamina obtained by extending by the MD unit cell periodically in two directions. The unidirectional nature of reinforcements makes the RVE more amenable to analysis as a transversely isotropic material. The stress-strain relation for a transversely isotropic material can be written in the Voigt notation as

$$\sigma_i = \mathbf{C}_{ij}\varepsilon_j \qquad i, j = 1, 2, \cdots 6 \tag{6}$$

where σ_i and ε_j = stress and strain, respectively, corresponding to the ith and jth indices; and $\mathbf{C}$ = stiffness matrix. The stress and strain vectors given by the Voigt notation corresponds to the components of the stress and strain tensors, respectively, as

$$\begin{aligned}
\sigma_{11} &= \sigma_1 & \varepsilon_{11} &= \varepsilon_1 \\
\sigma_{22} &= \sigma_2 & \varepsilon_{22} &= \varepsilon_2 \\
\sigma_{33} &= \sigma_3 & \varepsilon_{33} &= \varepsilon_3 \\
\sigma_{23} = \sigma_{32} &= \sigma_4 & 2\varepsilon_{23} = 2\varepsilon_{32} &= \gamma_{23} = \gamma_{32} = \varepsilon_4 \\
\sigma_{13} = \sigma_{31} &= \sigma_5 & 2\varepsilon_{13} = 2\varepsilon_{31} &= \gamma_{13} = \gamma_{31} = \varepsilon_5 \\
\sigma_{12} = \sigma_{21} &= \sigma_6 & 2\varepsilon_{12} = 2\varepsilon_{21} &= \gamma_{12} = \gamma_{21} = \varepsilon_6
\end{aligned} \tag{7}$$

Correspondingly, the components of the stiffness matrix are

$$\mathbf{C} = \begin{bmatrix}
\frac{(1-\nu_{13}\nu_{31})}{E_1E_3\Delta} & \frac{(\nu_{12}+\nu_{13}\nu_{31})}{E_1E_3\Delta} & \frac{(\nu_{13}+\nu_{12}\nu_{13})}{E_1E_3\Delta} & 0 & 0 & 0 \\
\frac{(\nu_{12}+\nu_{13}\nu_{31})}{E_1E_3\Delta} & \frac{(1-\nu_{13}\nu_{31})}{E_1E_3\Delta} & \frac{(\nu_{13}+\nu_{21}\nu_{13})}{E_1E_3\Delta} & 0 & 0 & 0 \\
\frac{(\nu_{31}+\nu_{21}\nu_{31})}{E_1E_1\Delta} & \frac{(\nu_{31}+\nu_{12}\nu_{31})}{E_1E_1\Delta} & \frac{(1-\nu_{12}\nu_{21})}{E_1E_1\Delta} & 0 & 0 & 0 \\
0 & 0 & 0 & G_{23} & 0 & 0 \\
0 & 0 & 0 & 0 & G_{23} & 0 \\
0 & 0 & 0 & 0 & 0 & \frac{E_1}{2(1+\nu_{12})}
\end{bmatrix} \tag{8}$$

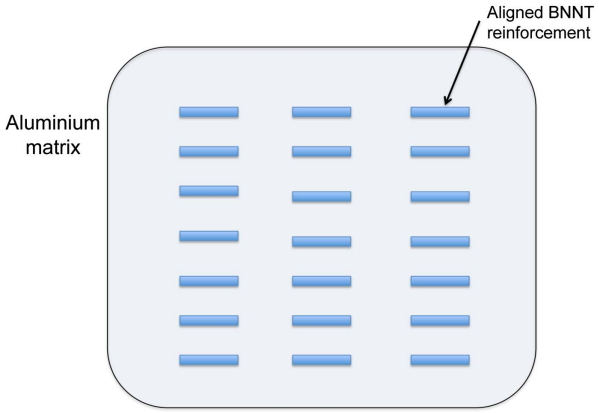

Fig. 3. Specially orthotropic lamina with the aligned BNNTs as reinforcement

where E_i = elastic modulus associated with direction i and is obtained by applying ε_i; and G_{ij} = shear modulus associated with ij plane and is obtained by applying $\varepsilon_{ij}, i \neq j$. Furthermore, Δ is given by

$$\Delta = \frac{(1+\nu_1)(1-\nu_1-2\nu_{13}\nu_{31})}{E_1^2 E_3} \tag{9}$$

Writing the constitutive law in terms of the compliance matrix decouples the equation and makes it less cumbersome. The compliance matrix, $\mathbf{S}$, is given by

$$\mathbf{S} = \mathbf{C}^{-1} = \begin{bmatrix} \frac{1}{E_1} & \frac{-\nu_{12}}{E_1} & \frac{-\nu_{13}}{E_3} & 0 & 0 & 0 \\ \frac{-\nu_{12}}{E_1} & \frac{1}{E_1} & \frac{-\nu_{13}}{E_3} & 0 & 0 & 0 \\ \frac{-\nu_{31}}{E_1} & \frac{-\nu_{31}}{E_1} & \frac{1}{E_3} & 0 & 0 & 0 \\ 0 & 0 & 0 & \frac{1}{G_{23}} & 0 & 0 \\ 0 & 0 & 0 & 0 & \frac{1}{G_{23}} & 0 \\ 0 & 0 & 0 & 0 & 0 & \frac{2(1+\nu_{12})}{E_1} \end{bmatrix} \tag{10}$$

Here $\nu_{ij} = \varepsilon_j/\varepsilon_i$ = Poisson's ratio. Although Eqs. (8) and (10) were derived assuming that the reinforcement direction is 1, in this paper the direction is 3. All subsequent equations are modified accordingly. Hence ν_{31} and ν_{13} denote the major and minor Poisson's ratios, respectively. Due to the symmetry of the $\mathbf{C}$ matrix, the Poisson's ratios are related to each other as $\nu_{12}/E_2 = \nu_{21}/E_1$ and $\nu_{13}/E_3 = \nu_{31}/E_1$. The constitutive relation for the RVE is defined completely once the unknowns $E_1, E_3, G_{23}, \nu_{12}$, and ν_{13} are evaluated. Thus if the unknowns are obtained using MD simulations, the constitutive relationship for the nanocomposite can be completely determined in a linear regime.

Analysis of a Specially Orthotropic Lamina

A specially orthotropic nanocomposite lamina can be obtained when the RVE is replicated in two orthogonal directions, one along (longitudinal) and the other perpendicular (transverse) to the length of the reinforcement. The analysis of this lamina can be simplified using a two-dimensional (2D) state of stress, or the plane stress assumption. Thus the constitutive relations given by Eq. (6) are simplified by substituting $\sigma_2 = \sigma_{23} = \sigma_{12} = 0$. The modified constitutive relation can be written as

$$\begin{Bmatrix} \varepsilon_1 \\ \varepsilon_3 \\ \varepsilon_{13} \end{Bmatrix} = \begin{bmatrix} \frac{1}{E_1} & \frac{-\nu_{31}}{E_3} & 0 \\ \frac{-\nu_{13}}{E_1} & \frac{1}{E_3} & 0 \\ 0 & 0 & \frac{1}{G_{13}} \end{bmatrix} \begin{Bmatrix} \sigma_1 \\ \sigma_3 \\ \sigma_{13} \end{Bmatrix} \tag{11}$$

Here, Direction 3 is parallel to the reinforcement and Direction 1 is perpendicular to the reinforcement. To study the orientation dependence of a composite with unidirectionally aligned fibers, let 1 and 2 be the axis perpendicular and 3 be the axis parallel to the reinforcement. Consider a uniaxial stress applied along the z direction at an angle θ from Axis 3 and $90^\circ - \theta$ from Axis 1. The elastic and shear moduli along with the Poisson's ratio of such a system can be obtained as (Gibson 2011)

$$\begin{aligned} E_z &= \left[\frac{1}{E_3}\cos^4\theta + \left(\frac{1}{G_{13}} - \frac{2\nu_{13}}{E_3}\sin^2\theta\cos^2\theta\right) + \frac{1}{E_1}\sin^4\theta\right]^{-1} \\ G_{zx} &= \left[\frac{1}{G_{13}}\left(\sin^4\theta + \cos^4\theta\right) + 4\left(\frac{1}{E_1} + \frac{1}{E_3} + \frac{2\nu_{13}}{E_3} - \frac{1}{G_{13}}\right)\sin^2\theta\cos^2\theta\right]^{-1} \\ \nu_{zx} &= E_z\left[\frac{\nu_{13}}{E_3}(\sin^4\theta + \cos^4\theta) - \left(\frac{1}{E_3} + \frac{1}{E_1} - \frac{1}{G_{13}}\right)\sin^2\theta\cos^2\theta\right] \end{aligned} \tag{12}$$

Normal strains can be generated from off-axis shear stresses, and vice-versa. This is known as the shear-coupling effect, and occurs due to the orientation of the reinforcement. For quantification, a dimensionless shear-coupling coefficient η is defined according to the state of stress. When $\sigma_z \neq 0$ and $\sigma_x = \sigma_{xz} = 0$, $\eta_{z,zx}$ is given by (Gibson 2011)

$$\begin{aligned} \eta_{z,zx} &= \frac{\gamma_{xy}}{\varepsilon_x} \\ &= E_z\left[\left(\frac{2}{E_3} + \frac{2\nu_{13}}{E_3} - \frac{1}{G_{13}}\right)\sin\theta\cos^3\theta \right. \\ &\quad \left. - \left(\frac{2}{E_1} + \frac{2\nu_{13}}{E_3} - \frac{1}{G_{13}}\right)\sin^3\theta\cos\theta\right] \end{aligned} \tag{13}$$

Rules of Mixtures

The effective elastic modulus of a composite—either aligned or randomly oriented reinforcement—can be given by a rule of mixtures. When the load is applied parallel to the fibers, the strains along the length of the fiber equal the strain in the matrix, $\varepsilon_f = \varepsilon_m = \varepsilon$. This assumption is valid only when there is a perfect bonding between the matrix and the reinforcement, which is not the case in reality. However, this assumption is useful to obtain upper and lower bounds for the elastic modulus of the composite, also known as the Voigt and Reuss limits, respectively. Hence, for loading parallel to the fiber axis

$$\sigma A = \sigma_f A_f + \sigma_m A_m$$
$$E_{\|}\varepsilon = E_{fa}\varepsilon_f \frac{A_f}{A} + E_m \varepsilon_m \frac{A_m}{A}$$
$$E_{\|} = E_{fa} V_f + E_m V_m \tag{14}$$

where V_f and V_m = volume fraction of the fiber and reinforcement, respectively, with $V_f + V_m = 1$; E_m = elastic modulus of the metal-matrix; and E_{fa} = elastic modulus of the fiber in the axial direction. Eq. (14) gives the upper limit of the elastic modulus of an aligned composite. Similarly, when the loading is orthogonal to the direction of reinforcement, the elastic modulus is

$$\frac{1}{E_{\perp}} = \frac{V_f}{E_{fr}} + \frac{V_m}{E_m} \tag{15}$$

where E_{fr} = elastic modulus of the fiber in the radial direction. Typically the elastic moduli in axial and radial directions are equal for the fiber, that is, $E_{fa} = E_{fr} = E_f$. Eq. (15) gives the lower limit of the elastic modulus of an aligned composite. However, when the fibers are randomly oriented an almost isotropic behavior follows. In this case a useful engineering approximation (Tsai 1964; Gibson 2011) of the elastic modulus is

$$E \approx (3/8)E_{\perp} + (5/8)E_{\|} \tag{16}$$

where $E_{\perp}$ and $E_{\|}$ = the upper (Voigt) and lower (Reuss) limits, respectively. Variation of all these parameters is studied in detail in the next section.

Results and Discussions

Results of RVE

Fig. 4 plots variations of stress with the applied strain under different loading conditions. As mentioned previously, uniaxial compressive and shear loadings are applied to the RVE separately to obtain the elastic and shear moduli and the Poisson's ratios in the respective directions.

For a compressive loading in the axial direction, Fig. 4(a) plots the stress as a function of the applied strain. The elastic modulus of a BNNT-reinforced aluminum matrix shows improvement compared with the pure aluminum. Although there was no significant change in the elastic modulus, the failure strength increased with the number of walls of the nanotube. The reinforcement enhanced the properties of the matrix in the axial direction.

Fig. 4(b) plots the response of nanocomposite to uniaxial compression orthogonal to the reinforcement. The failure strength of the nanocomposite was lower than that of the pure aluminum under uniaxial compression in the transverse direction. Nanotubes are known to be weak in the radial direction due to their hollow cylindrical structure (Zheng 2012a; Zheng et al. 2012b). When compressive loading is applied in the transverse direction, nanotubes compress radially, leading to failure. This weakness of nanotubes under radial loading makes a nanocomposite weaker in the transverse direction. However, the elastic modulus in the transverse direction was not significantly lower than that of pure aluminum. In the linear regime, the transverse elastic modulus of pure aluminum

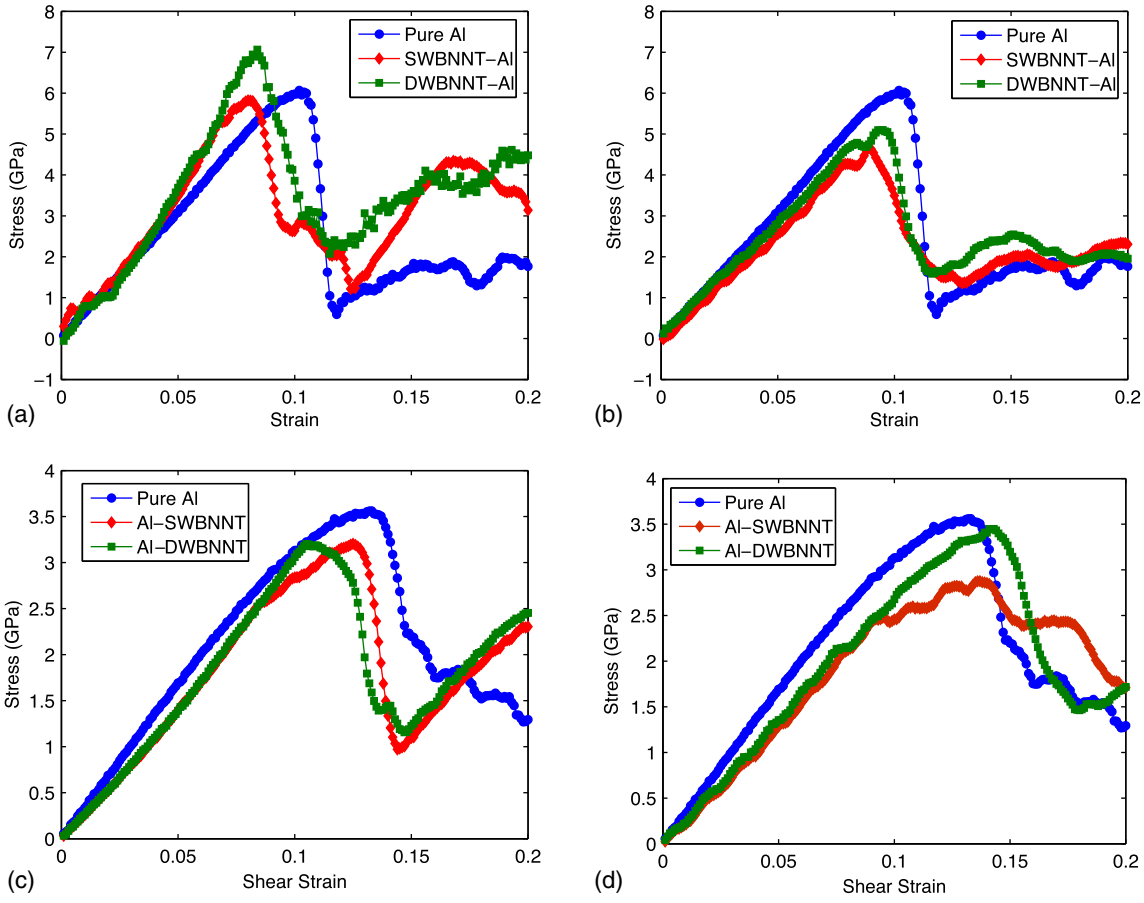

Fig. 4. Stress versus strain plot of the RVE of pure aluminum, SWBNNT-reinforced nanocomposite, and DWBNNT-reinforced nanocomposite under different loading conditions: (a) normal strain in longitudinal direction; (b) normal strain in transverse direction; (c) shear strain in 13 direction; (d) shear strain in 12 direction

and the nanocomposite matched closely. Therefore, even though there was a reduction in the strength of the nanocomposite in the transverse direction, the stiffness of the nanocomposite was not compromised compared with pure aluminum.

Figs. 4(c and d) plot the response of the nanocomposite under applied shear strains. The shear strain was applied separately in the 13 and the 12 directions. When the shear load was applied in the 13 or 23 direction, the tube underwent bending. However, when the shear load was applied in the 12 direction, the tube underwent nonuniform radial deformation, leading to distorted shapes.

The stiffness of the nanocomposite was lower than the stiffness of pure aluminum under the application of shear strains ε_{13} and ε_{12}. The shear modulus corresponding to a strain in the 13 direction was comparable to that of pure aluminum. Especially in the case of a DWBNNT reinforcement, the stress-strain curve intersected with that of pure aluminum, as shown in Fig. 4. However, the failure strength was slightly lower than that of pure aluminum for both SWBNNT and DWBNNT reinforcements.

When the strain was applied in the 12 direction, the tube underwent a radial deformation. Because the nanotubes are weaker in the radial direction, the shear modulus G_{12} for nanocomposite is lower than for pure aluminum. The effect of the number of walls on the strength of the composite is visible in this case. The DWBNNT-nanocomposite exhibited the same strength as pure aluminum, although with a lower stiffness. However, a SWBNNT-nanocomposite exhibited a relatively lower failure strength, as plotted in Fig. 4(d).

Furthermore, the failure mechanisms in each of the loading cases were studied by observing the atomic trajectories obtained from the MD simulations. The failure in the case of longitudinal normal loading occurred due to the failure of the matrix, which further led to the buckling of the tube. Because DWBNNT is stronger in compression against buckling, RVE with DWBNNT exhibited greater strength than the RVE with SWBNNT. Under transverse loading, the failure was governed by the nanotubes. Because of their weakness in the radial direction, the nanotubes failed by buckling when the aluminum matrix pushed against the walls of nanotubes under transverse normal loading. Under shear loading, the failure always occurred at the interface. The weakness of the interface to transfer the load effectively resulted in the shearing of the interface, leading to the failure of the aluminum near the interface. Thus, depending on the type of loading, all three cases of failure—nanotube, matrix, and interface—were observed. Hence it is noted that when designing a nanocomposite, all three loading cases need to be considered.

Overall, reinforcing the aluminum matrix with BNNTs made the nanocomposite directionally stronger. In fact, using nanotubes with more walls might make the composite even stronger. Hence a DWBNNT is preferred over a SWBNNT as reinforcement. Table 2 presents the computed elastic and shear moduli and Poisson's ratios. The failure strengths corresponding to the respective directions of applied strains also are presented in this table. These values can be used to describe the constitutive relation of the RVE of the nanocomposite as given by Eqs. (6) and (8). One other interesting observation in Fig. 4 is that often there is a postfailure increase in the stress-strain plot. After the failure of the matrix, the reinforcement takes the entire applied load. The stiffness of the reinforcement also contributes to the increase in the stress-strain plot.

Results on Bulk Nanocomposite

The results obtained from MD can be directly used for a laminar nanocomposite with aligned reinforcement. However, these properties are for loading either along or orthogonal to the reinforcement direction. A nanocomposite lamina with aligned reinforcements might undergo loads in directions at an angle to the reinforcement as well. To generalize the result, it is essential to know the constitutive relationship in the nonprincipal coordinates, also known as off-axis coordinates. The integration of off-axis properties for the orientation angle θ can further yield results for randomly oriented nanocomposite.

Table 2. Elastic Modulus, Poisson's Ratio, and Failure Strength Obtained from the MD Simulations

Property	Pure Al	SWBNNT	DWBNNT
E_1 (GPa)	59.75	52.373	59.471
E_3 (GPa)	59.471	72.775	84.112
G_{13} (GPa)	32.887	30.508	30.508
ν_{12}	0.32	0.31	0.31
ν_{13}	0.32	0.35	0.36
$\sigma_{1,ult}$[a] (GPa)	5.975	4.661	5.099
$\sigma_{3,ult}$ (GPa)	6.066	5.822	7.066
$\sigma_{13,ult}$ (GPa)	3.558	3.203	3.203

[a]Subscript ult refers to the ultimate strength along the given direction of applied strain.

Off-Axis Properties

Using the laminar mechanics of a composite, the off-axis properties can be obtained using Eqs. (12) and (13). The values of E_1, E_3, G_{13}, and ν_{13} were obtained from MD simulations given in Table 2. Fig. 5 plots the variation of elastic and shear moduli, Poisson's ratio, and shear-coupling coefficient with lamina orientation.

An interesting observation in Fig. 5(a) is that the stiffness E_3 does not decrease for slight changes in the angle of loading θ. The increased elastic modulus E_3 is maintained, which gradually reduces to the elastic modulus E_1. Therefore aligned reinforcement of nanotubes is effective in imparting improved stiffness to the nanocomposite. This happens not just along the reinforcement but even at angles significantly greater than 0°. This is in contrast to traditional fiber reinforcement composite, in which the elastic stiffness decreases suddenly for a small increase in θ (Gibson 2011). Similarly, Fig. 5(b) plots the variation of shear modulus. As expected, the shear modulus increases with θ to 45° and then gradually decreases to the same value as at 0° and 90°. The DWBNNT reinforcement significantly enhances the shear modulus compared with SWBNNT. This observation further substantiates the previous deduction that the DWBNNT can provide stiffer reinforcement for nanocomposite.

Rules of Mixtures

When manufacturing a nanocomposite, it is challenging to place all nanotubes in an aligned orientation. Generally, nanotube reinforcements are oriented in random directions, yielding a nearly isotropic nanocomposite. Mechanical properties of this nanocomposite can be obtained by integrating the off-axis elastic modulus with respect to the orientation angle. The upper and lower limits for the elastic modulus are given by Eqs. (14) and (15), respectively. First consider the usual composite theory in which $E_{fa} = E_{fr}$. Values of E_{fa} (Krishnan and Ghosh 2014) and E_m were substituted in these equations. Fig. 6(a) plots the variation of the elastic moduli with the volume fraction (in percentage). In this figure the upper and lower bounds are marked as UB-composite and LB-composite, respectively. However, for tubular structures, $E_{fr} \ll E_{fa}$. Particularly for BNNT, the difference is of two orders of magnitude. Thus E_{fa} and E_{fr} were obtained from the literature (Zheng 2012a; Zheng et al. 2012b) and substituted in Eqs. (14) and (15), and also are plotted in Fig. 6(a). This is referred to as the modified mixture rule. In addition, whereas the upper and lower bounds of the conventional

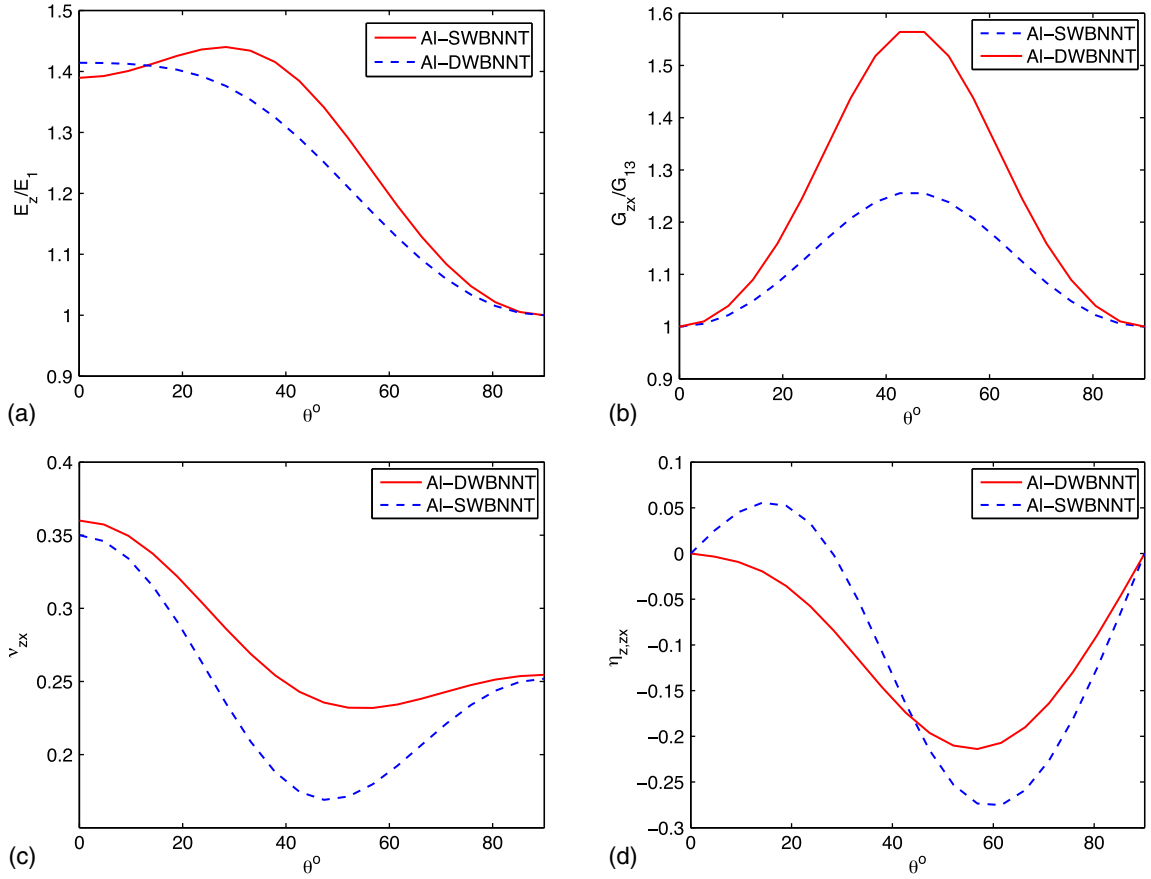

Fig. 5. Variation with orientation of the reinforcement in a nanocomposite of the (a) elastic modulus; (b) shear modulus; (c) Poisson's ratio; (d) shear-coupling coefficient

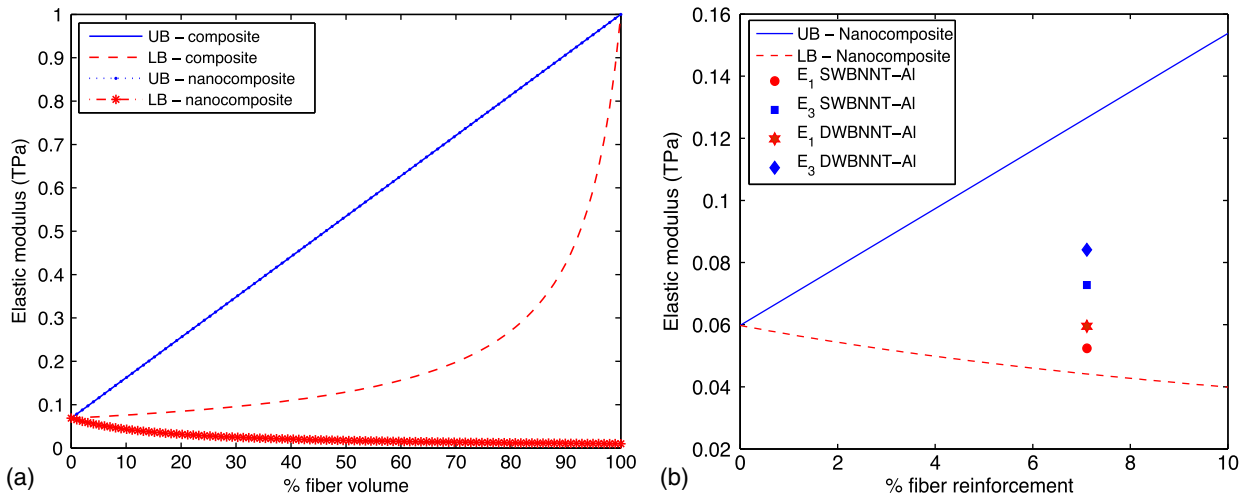

Fig. 6. (a) Variation of the elastic modulus with the percentage fiber reinforcement; UB and LB correspond to the upper bound and lower bound, respectively; (b) the values obtained from simulation compared with predicted upper and lower limit considering the nanotube reinforcement

mixture rule converge for 100% fiber volume, the bounds diverged significantly in the case of nanotubes. This divergence is due to the radial weakness of nanotubes. For nanotubes to behave like a conventional fiber composite, the radial stiffness (E_{fr}) should be equal to the longitudinal stiffness (E_{fa}). These upper and lower bounds are marked in Fig. 6(a) as UB-nanocomposite and LB-nanocomposite, respectively. The conventional composite theory overestimates the lower bound, whereas the upper bound is preserved. The actual stiffness of a nanocomposite will lie anywhere between these modified upper and lower limits. These limits are verified against results obtained from MD simulations in Fig. 6(b). However, note that the MD results lie considerably below the modified upper bound. This difference can be attributed to the fact that an actual interface, which is modeled well by an LJ

J. Nanomech. Micromech., 2017, 7(4): 04017014

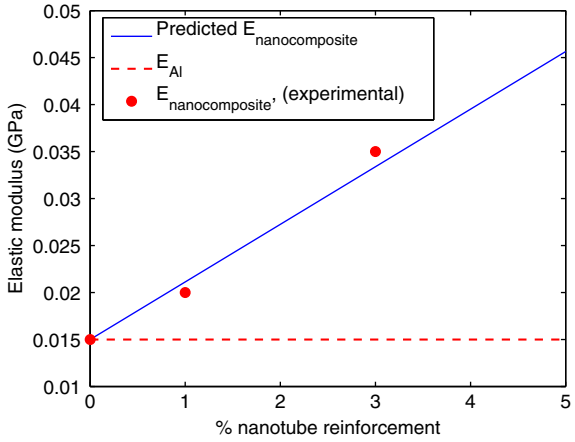

Fig. 7. Comparison of mixture rule with results of Yamaguchi et al. (2013)

potential, is weaker than an ideal perfect bonding assumed by the upper bound.

To test the validity of the modified mixture rule further, predictions were compared with the experimental results obtained (Yamaguchi et al. 2013). Using Eq. (16) with the modified mixture rule, Fig. 7 plots the stiffness of nanocomposite with randomly oriented reinforcement. The values obtained by Yamaguchi et. al. are plotted corresponding to their percentage of nanotube reinforcement. The comparison shows that the modified mixture rule can accurately predict the elastic modulus of nanocomposites. The key factor here is the difference between axial and radial elastic moduli of reinforcements, which was ignored in previous studies.

Concluding Remarks

The following major conclusions can be drawn from this paper:

1. The transverse isotropy assumption at the RVE level leads to stiffness estimates of the bulk nanocomposite comparable to experimental and molecular simulation results.
2. Depending on the type of loading, the failure of a nanocomposite can occur due to the failure of reinforcement, matrix, or interface. Thus it is important consider all three cases while designing a composite.
3. The modified mixture rule, which is developed based on a hierarchical multiscale scheme, provides better bounds of the stiffness.
4. The radial weakness of nanotubes affects the stiffness of the nanocomposite. This weakness can be partially compensated for by increasing the number of walls. Further research is required to incorporate this enhancement in a multiscale scheme.

Moreover, the present study can be extended to model the failure of nanocomposites under tensile loading with special attention to the stress transfer between the nanotube and the matrix during pull-out simulations, and associated shear lag. Such studies can provide a qualitative and quantitative analysis of the effectiveness of nanocomposites for practical applications.

Acknowledgments

The authors thank the Board of Research in Nuclear Sciences (BRNS) Grant No. 2012/36/37-BRNS/ 1683 for financial support.

References

Ajayan, P. M., Schadler, L. S., and Braun, P. V. (2006). *Nanocomposite science and technology*, Wiley, NJ.

Allen, M. P., et al. (1987). *Computer simulation of liquids*, Clarendon press Oxford, Oxford, U.K.

Bakshi, S., Lahiri, D., and Agarwal, A. (2010). "Carbon nanotube reinforced metal matrix composites—A review." *Int. Mater. Rev.*, 55(1), 41–64.

Bernhardt, D. J. (2014). "Composite reinforcement using boron nitride nanotubes." Queensland Univ., Brisbane, Australia.

Camargo, P. H. C., Satyanarayana, K. G., and Wypych, F. (2009). "Nanocomposites: Synthesis, structure, properties and new application opportunities." *Mater. Res.*, 12(1), 1–39.

Coleman, J. N., Khan, U., Blau, W. J., and Gunko, Y. K. (2006). "Small but strong: A review of the mechanical properties of carbon nanotube-polymer composites." *Carbon*, 44(9), 1624–1652.

Delley, B. (1990). "An all-electron numerical method for solving the local density functional for polyatomic molecules." *J. Chem. Phys.*, 92(1), 508–517.

Delley, B. (2000). "From molecules to solids with the DMol3 approach." *J. Chem. Phys.*, 113(18), 7756–7764.

Esawi, A., and Morsi, K. (2007). "Dispersion of carbon nanotubes (CNTs) in aluminum powder." *Compos. Part A: Appl. Sci. Manuf.*, 38(2), 646–650.

Fish, J. (2009). *Multiscale methods: Bridging the scales in science and engineering*, Oxford University Press, Oxford, U.K.

George, R., Kashyap, K., Rahul, R., and Yamdagni, S. (2005). "Strengthening in carbon nanotube/aluminium (CNT/Al) composites." *Scr. Mater.*, 53(10), 1159–1163.

Gibson, R. F. (2011). *Principles of composite material mechanics*, CRC Press, Boca Raton, FL.

Gojny, F. H., Wichmann, M., Köpke, U., Fiedler, B., and Schulte, K. (2004). "Carbon nanotube-reinforced epoxy-composites: Enhanced stiffness and fracture toughness at low nanotube content." *Compos. Sci. Technol.*, 64(15), 2363–2371.

Han, Y., Jing, H., Nai, S., Xu, L., Tan, C. M., and Wei, J. (2012). "Creep mitigation in Sn–Ag–Cu composite solder with Ni-coated carbon nanotubes." *J. Mater. Sci. Mater. Electron.*, 23(5), 1108–1115.

He, C., et al. (2007). "An approach to obtaining homogeneously dispersed carbon nanotubes in Al powders for preparing reinforced Al-matrix composites." *Adv. Mater.*, 19(8), 1128–1132.

He, C., Zhao, N., Shi, C., and Song, S. (2009). "Mechanical properties and microstructures of carbon nanotube-reinforced Al matrix composite fabricated by in situ chemical vapor deposition." *J. Alloys Compd.*, 487(1), 258–262.

Herasati, S., and Zhang, L. (2014). "A new method for characterizing and modeling the waviness and alignment of carbon nanotubes in composites." *Compos. Sci. Technol.*, 100(0), 136–142.

Humphrey, W., Dalke, A., and Schulten, K. (1996). "VMD: Visual molecular dynamics." *J. Mol. Graphics*, 14(1), 33–38.

Ivashchenko, V., Veprek, S., Pogrebnjak, A., and Postolnyi, B. (2014). "First-principles quantum molecular dynamics study of TixZr1–xN (111)/SiNy heterostructures and comparison with experimental results." *Sci. Technol. Adv. Mater.*, 15(2), 025007.

Kim, C., Rohatgi, P., and Sanaty-Zadeh, A. (2011). "Multi-scale modeling on the mechanical behavior of aluminum-based metal-matrix nanocomposites (MMNCs)." Minerals, Metals and Materials Society/AIME, Warrendale, PA.

Kim, K. T., Cha, S. I., and Hong, S. H. (2007). "Hardness and wear resistance of carbon nanotube reinforced Cu matrix nanocomposites." *Mater. Sci. Eng. A*, 449, 46–50.

Krishnan, N. M. A., and Ghosh, D. (2014). "Chirality dependent elastic properties of single-walled boron nitride nanotubes under uniaxial and torsional loading." *J. Appl. Phys.*, 115(6), 064303.

Krishnan, N. M. A., and Ghosh, D. (2014). "Defect induced plasticity and failure mechanism of boron nitride nanotubes under tension." *J. Appl. Phys.*, 116(4), 044313.

Lahiri, D., et al. (2012). "Insight into reactions and interface between boron nitride nanotube and aluminum." *J. Mater. Res.*, 27(21), 2760–2770.

Lahiri, D., et al. (2013). "Boron nitride nanotubes reinforced aluminum composites prepared by spark plasma sintering: Microstructure, mechanical properties and deformation behavior." *Mater. Sci. Eng. A*, 574, 149–156.

Li, Y., Zhou, Z., Golberg, D., Bando, Y., Schleyer, P. v. R., and Chen, Z. (2008). "Stone-Wales defects in single-walled boron nitride nanotubes: Formation energies, electronic structures, and reactivity." *J. Phys. Chem. C*, 112(5), 1365–1370.

Liu, W., Karpov, E., and Park, H. (2006). *Nano mechanics and materials: Theory, multiscale methods and applications*, Wiley, NJ.

Miller, R. E., and Tadmor, E. (2009). "A unified framework and performance benchmark of fourteen multiscale atomistic/continuum coupling methods." *Modell. Simul. Mater. Sci. Eng.*, 17(5), 053001.

Moon, W. H., and Hwang, H. J. (2004). "Molecular-dynamics simulation of structure and thermal behaviour of boron nitride nanotubes." *Nanotechnol.*, 15(5), 431–434.

Noguchi, T., et al. (2004). "Carbon nanotube/aluminium composites with uniform dispersion." *Mater. Trans.*, 45(2), 602–604.

Perdew, J. P., Burke, K., and Ernzerhof, M. (1996). "Generalized gradient approximation made simple." *Phys. Rev. Lett.*, 77(18), 3865–3868.

Plimpton, S. (1995). "Fast parallel algorithms for short-range molecular dynamics." *J. Comput. Phys.*, 117(1), 1–19.

Pogrebnjak, A. D., and Beresnev, V. M. (2012). *Nanocoatings nanosystems nanotechnologies*, Bentham Science Publishers, United Arab Emirates.

Pogrebnjak, A. D., Borisyuk, V. N., Bagdasaryan, A. A., Maksakova, O. V., and Smirnova, E. V. (2014). "The multifractal investigation of surface microgeometry of (Ti–Hf–Zr–V–Nb)N nitride coatings." *J. Nano Electron. Phys.*, 6(4), 4018-1.

Porwal, H., Grasso, S., and Reece, M. (2013). "Review of graphene-ceramic matrix composites." *Adv. Appl. Ceram.*, 112(8), 443–454.

Sekkal, W., Bouhafs, B., Aourag, H., and Certier, M. (1998). "Molecular-dynamics simulation of structural and thermodynamic properties of boron nitride." *J. Phys. Condens. Matter*, 10(23), 4975–4984.

Sevik, C., Kinaci, A., Haskins, J. B., and Çağın, T. (2011). "Characterization of thermal transport in low-dimensional boron nitride nanostructures." *Phys. Rev. B*, 84(8), 085409.

Silvestre, N. (2013). "State-of-the-art review on carbon nanotube reinforced metal matrix composites." *Int. J. Compos. Mater.*, 3(6A), 28–44.

Silvestre, N., Faria, B., and Canongia Lopes, J. N. (2014). "Compressive behavior of CNT-reinforced aluminum composites using molecular dynamics." *Compos. Sci. Technol.*, 90, 16–24.

Song, H.-Y., and Zha, X.-W. (2010). "Influence of nickel coating on the interfacial bonding characteristics of carbon nanotube-aluminum composites." *Comput. Mater. Sci.*, 49(4), 899–903.

Subramaniyan, A. K., and Sun, C. (2008). "Continuum interpretation of virial stress in molecular simulations." *Int. J. Solids Struct.*, 45(14), 4340–4346.

Tsai, S. W. (1964). "Structural behavior of composite materials." Philco-Ford Corporation, Newport Beach, CA.

Winey, J., Kubota, A., and Gupta, Y. (2009). "A thermodynamic approach to determine accurate potentials for molecular dynamics simulations: Thermoelastic response of aluminum." *Modell. Simul. Mater. Sci. Eng.*, 17(5), 055004.

Yamaguchi, M., et al. (2013). "Utilization of multiwalled boron nitride nanotubes for the reinforcement of lightweight aluminum ribbons." *Nanoscale Res. Lett.*, 8(1), 3–6.

Yamaguchi, M., Tang, D.-M., Zhi, C., Bando, Y., Shtansky, D., and Golberg, D. (2012). "Synthesis, structural analysis and in situ transmission electron microscopy mechanical tests on individual aluminum matrix/boron nitride nanotube nanohybrids." *Acta Mater.*, 60(17), 6213–6222.

Yang, J., Zhang, Z., Friedrich, K., and Schlarb, A. K. (2007). "Creep resistant polymer nanocomposites reinforced with multi-walled carbon nanotubes." *Macromol. Rapid Commun.*, 28(8), 955–961.

Zhan, G.-D., Kuntz, J. D., Wan, J., and Mukherjee, A. K. (2003). "Single-wall carbon nanotubes as attractive toughening agents in alumina-based nanocomposites." *Nature Mater.*, 2(1), 38–42.

Zheng, M., et al. (2012a). "Radial mechanical properties of single-walled boron nitride nanotubes." *Small*, 8(1), 116–121.

Zheng, M., Ke, C., Bae, I., Park, C., Smith, M., and Jordan, K. (2012b). "Radial elasticity of multi-walled boron nitride nanotubes." *Nanotechnol.*, 23(9), 095703.

Zobelli, A., Ewels, C., Gloter, A., and Seifert, G. (2007). "Vacancy migration in hexagonal boron nitride." *Phys. Rev. B*, 75(9), 094104.